Harvesting hot holes in plasmon-coupled ultrathin photoanodes for high-performance photoelectrochemical water splitting

Vahidzadeh, Ehsan; Zeng, Sheng; Alam, Kazi M.; Kumar, Pawan; Riddell, Saralyn; Chaulagain, Narendra; Gusarov, Sergey; Kobryn, Alexander E.; Shankar, Karthik

Publisher's version / Version de l'éditeur:
https://doi.org/10.1021/acsami.1c10698
ACS Applied Materials & Interfaces, 13, 36, pp. 42741-42752, 2021-09-03

Harvesting Hot Holes in Plasmon-coupled Ultrathin Photoanodes for High-Performance Photoelectrochemical Water Splitting

Ehsan Vahidzadeh,[1] Sheng Zeng,[1] Kazi M Alam,[1,2] Pawan Kumar,[1†] Saralyn Riddell,[1] Narendra Chaulagain,[1] Sergey Gusarov,[2] Alexander E. Kobryn[2] and Karthik Shankar[1]*

[1]Department of Electrical and Computer Engineering, University of Alberta, 9211 - 116 St, Edmonton, AB T6G 1H9, Canada.

[2]Nanotechnology Research Centre, National Research Council of Canada, Edmonton, Alberta, Canada

ABSTRACT: The harvesting of hot carriers produced by plasmon decay to generate electricity or drive a chemical reaction enables reduction of the thermalization losses associated with supra-bandgap photons in semiconductor photoelectrochemical (PEC) cells. Through the broadband harvesting of light, hot carrier PEC devices also produce a sensitizing effect in heterojunctions with wide bandgap metal oxide semiconductors possessing good photostability and catalytic activity but poor absorption of visible wavelength photons. There are several reports of hot electrons in Au injected over the Schottky barrier into crystalline TiO_2 and subsequently utilized to drive a chemical reaction but very few reports of hot hole harvesting. In this work, we

demonstrate the efficient harvesting of hot holes in Au nanoparticles covered with a thin layer of amorphous TiO_2 (a-TiO_2). Under AM1.5 one sun illumination, photoanodes consisting of a single layer of ~50 nm diameter Au NPs coated with a 10 nm shell of amorphous TiO_2 (Au@a-TiO_2) generated 2.5 mA cm^{-2} of photocurrent in 1 M KOH under 0.6 V external bias, rising to 3.7 mA cm^{-2} in the presence of a hole scavenger (methanol). The quantum yield for hot carrier-mediated photocurrent generation was estimated to be close to unity for high energy photons ($\lambda < 420$ nm). Au@a-TiO_2 photoelectrodes produced a small positive photocurrent of 0.1 mA cm^{-2} even at a bias of -0.6 V indicating extraction of hot holes even at strong negative bias. These results together with density functional theory (DFT) modeling and scanning Kelvin probe force microscope (KPFM) data indicate fast injection of hot holes from Au NPs into a-TiO_2 and light harvesting performed near-exclusively by Au NPs. For comparison, Au NPs coated with a 10 nm shell of Al_2O_3 (Au@Al_2O_3) generated 0.02 mA cm^{-2} of photocurrent in 1 M KOH under 0.6 V external bias. These results underscore the critical role played by amorphous TiO_2 in extraction of holes in Au@a-TiO_2 photoanodes, which is not replicated by an ordinary dielectric shell. It is also demonstrated here that an ultrathin photoanode (< 100 nm in maximum thickness) can efficiently drive sunlight-driven water splitting.

KEYWORDS: Plasmonic photocatalysis; FDTD electromagnetic simulations; spontaneous dewetting; artificial photosynthesis; interband damping

1. INTRODUCTION

The production of solar fuels using semiconductor photocatalysts and photoelectrodes has been investigated since the early 1970s.[1, 2] Photochemically stable, catalytically active semiconductors such as TiO_2, $SrTiO_3$, GaN, g-C_3N_4, etc have wide bandgaps and therefore primarily harvest blue and ultraviolet photons while wasting (through lack of absorption) a large number of lower energy

photons capable of driving chemical reactions of interest such as H_2 generation from water and photoreduction of CO_2 into value-added hydrocarbons. Moderate bandgap and narrow bandgap semiconductors such as Cu_2O, Si, GaP, CdS, etc experience photocorrosion and some even have poor catalytic activity. Another inherent problem associated with semiconductor catalysts is the thermalization loss associated with the relaxation of more energetic charge carriers excited by supra-bandgap photons to the bottom of the conduction band before participating in desired redox processes.

Recently, there has been increasing interest in plasmonic catalysis to circumvent these limitations.[3-5] Plasmonic catalysis offers the potential of driving a wide variety of chemical reactions close to room temperature by harnessing the intense light matter interaction, fast charge transfer and strong vibrational coupling to adsorbates exhibited by select plasmonic nanoparticles. Plasmonic catalysis can be predominantly carrier-driven or phonon-driven. Nanoparticles made of a select group of materials that includes Ag, Au, Cu, Al and certain transition metal nitrides, exhibit localized surface plasmon resonances (LSPR) at visible wavelengths.[6, 7] The LSPR phenomenon consists of the coherent and collective oscillations of conduction band electrons at nanoparticle-dielectric interfaces (surface plasmons) excited by incident photons. Surface plasmons dephase in 3-30 femtoseconds through either radiative damping (which results in re-emission of the photon) or through non-radiative damping processes such as surface scattering, Landau (intraband) damping, interband damping and chemical interface damping, which result in the creation of hot carrier pairs.[8, 9] The statistics of the geminate electrons and holes formed by plasmon decay follow a Fermi-Dirac distribution corresponding a large effective electron temperature compared to room temperature due to which these carriers are said to be "hot'.[9] Furthermore, the energies of the geminate hot carriers are not necessarily evenly distributed. In gold nanoparticles, the hot holes

have higher effective temperatures than the hot electrons.[10] The key goal in carrier-driven plasmonic catalysis is to utilize the excess energy of hot carriers to drive a chemical reaction before they are lost to thermal relaxation or electron-hole recombination.

The utilization of hot carriers in plasmonic catalysts presents a particular challenge due to the ultrafast nature of relaxation processes and the poor catalytic activity of plasmonic noble metal surfaces.[3, 11] Hot carriers lose energy by electron-electron collisions in < 100 fs and experience phonon scattering in ~ 1 ps.[12] A number of research reports have shown that hot electrons in Au can be injected across a Schottky barrier formed in a heterojunction with a catalytically active, wide bandgap *n*-type semiconductor, before the thermal equilibration.[5] Such hot electron heterojunction photocatalysts have been used to perform CO_2 photoreduction, nitrobenzenethiol photoreduction, photoreduction of bicarbonate, etc.[13-17] On the other hand, there are very few reports on the harvesting of hot holes in plasmonic catalysts. Even rarer are reports on high performance photovoltaic or photoelectrochemical devices that rely on the extraction of hot holes from Au NPs. A fundamental problem is that Schottky barriers across which hot holes can be injected, typically form between *p*-type semiconductors and low work-function metals. Since gold is a high work function metal, it tends to form ohmic contacts with *p*-type semiconductors and renders it rather difficult to construct hot hole-harvesting Schottky junctions. Recent attempts at using organic hole transport layers to extract hot holes from Au NPs reported photocurrent densities <100 μAcm^{-2} under solar illumination.[18] We present an unorthodox solution to the aforementioned problem of hot hole extraction from Au NPs. Our approach makes use of amorphous TiO_2 as a hole collection layer and is successful in generating photocurrents approaching 4 $mAcm^{-2}$ in methanol-containing KOH electrolyte under AM1.5G one sun illumination.

2. RESULTS AND DISCUSSION

2.1 Structure, composition and optical properties of Au@a-TiO_2 photoanode

We formed a single layer of hemispherical gold nanoislands (~50 nm average diameter) on fluorine-doped tin oxide (FTO) coated glass substrates by vacuum deposition followed by spontaneous thermal dewetting. The He ion micrograph in Figure 1a provides evidence that annealing at 550 ℃ was successful in dewetting the sputtered gold film. The morphology and size distribution of the Au nanoislands are shown in Figure S2a in Supporting Information. The Au NPs were coated with a ~10 nm layer of amorphous TiO_2 (a-TiO_2) using atomic layer deposition (ALD). The clear distinction between the Au (core) and TiO_2 (shell) in the core-shell structure of the fabricated photoelectrode is clearly shown in the Helium ion images of Au@a-TiO_2 (Figure 1b). Following the dewetting, the surface of FTO was exposed in the inter-nanoisland gaps. Since ALD is a cyclic, conformal, and precise deposition process, the deposition of a-TiO_2 on the hemispherical Au nanoislands formed a shell around the gold core and also completely covered the exposed surface of FTO in the Au@a-TiO_2 sample (Figure S2b).

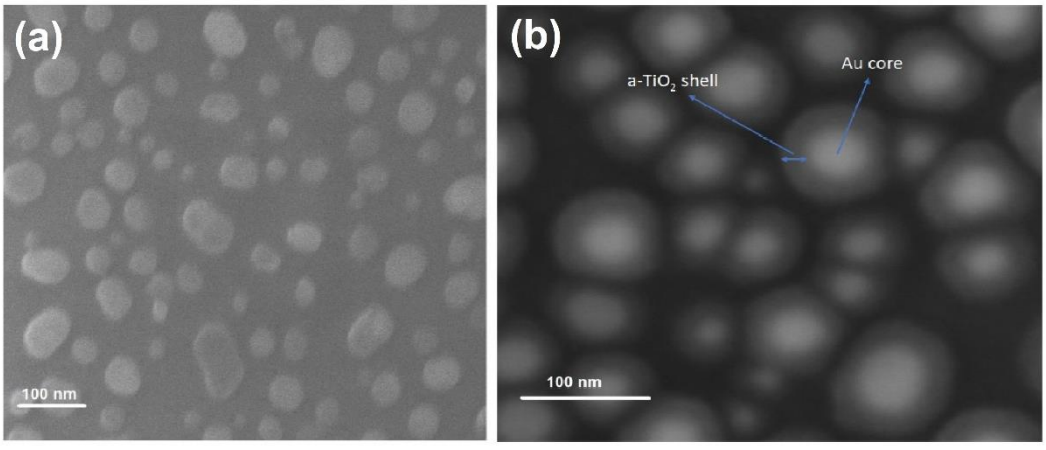

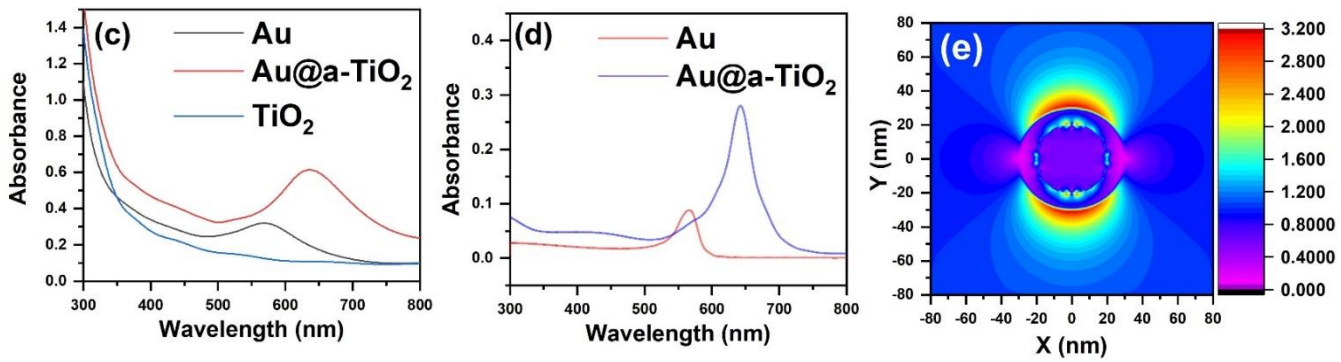

Figure 1. Helium ion images of (a) Au and (b) Au@TiO_2 on the glass substrate. (c) UV-Vis spectrum of Au, a-TiO_2, and Au@a-TiO_2 and (d) FDTD simulated absorption cross-section of Au and Au@a-TiO_2 (e) Top view electric field profile of Au@a-TiO_2 under 650 nm excitation.

The UV-Vis spectrum of the Au sample (indicated by a solid black line) exhibits a peak at around 560 nm (Figure 1c), which is the characteristic LSPR peak of 50 nm Au NPs bounded by air and FTO:glass, which is accurately reproduced by the finite difference time domain (FDTD) electromagnetic simulation result (red curve in Figure 1d). It is well-known that the plasmon resonance is exquisitely sensitive to the permittivity of the medium surrounding the metal. The LSPR peak of Au shifted from 560 nm to 650 nm after deposition of the a-TiO_2 shell (red curve in Figure 1c) which is attributable to the much higher refractive index of a-TiO_2 compared to air, thus shifting the Fröhlich resonance condition to longer wavelengths. The dramatic red-shift of the LSPR to 650 nm is also captured by the FDTD simulated absorption cross-section of the Au@a-TiO_2 sample (blue curve in Figure 1d). The FDTD simulations were performed for isolated Au NPs and ignored the effect of polydispersity-induced inhomogeneous broadening present in real samples. Consequently, the FDTD simulated spectra in Figure 1d show narrower peaks than the measured spectra in Figure 1c. The sharp rise in absorption for wavelengths below 350 nm in the measured spectra (Figure 1c) is due to the absorption edge of the FTO substrate, which is a degenerately doped semiconductor. The 10 nm TiO_2 coating contributes very little to the observed absorption. The FDTD simulated cross-section of the electric field distribution for a single Au@a-

TiO_2 particle excited at resonance (650 nm) demonstrates a strong local field enhancement at the interface between the Au NPs and the a-TiO_2 shell.

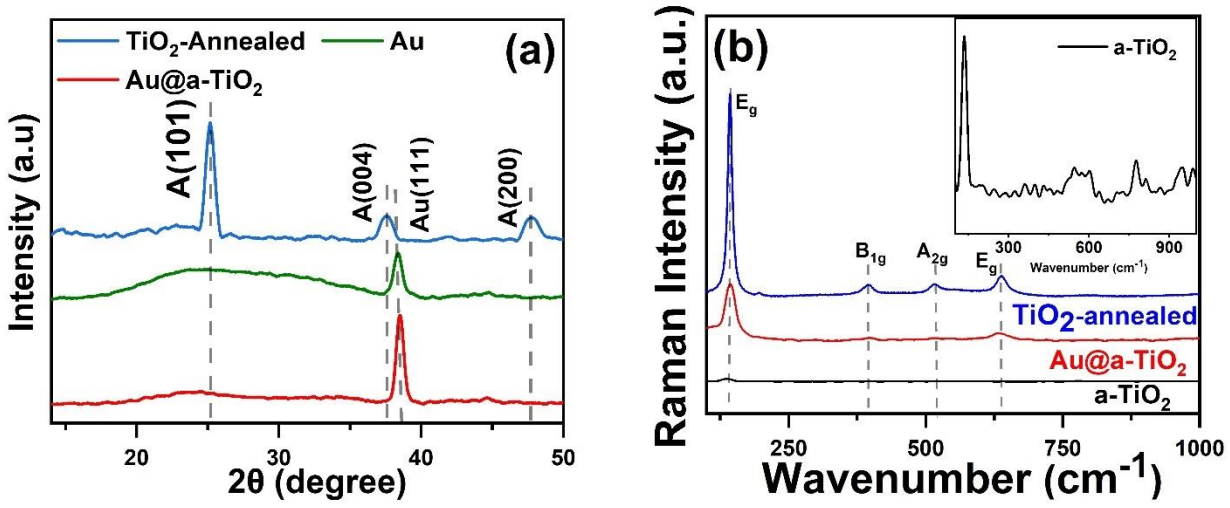

Figure 2. (a) XRD patterns of gold, annealed crystalline TiO_2 and Au@a-TiO_2. The Au@a-TiO2 core-shell nanoparticlesRaman spectra of a-TiO2, Au@a-TiO2 and annealed a-TiO_2. The substrate was FTO-coated glass in each case.

The x-ray diffraction (XRD) patterns of Au (green line in Figure 2a) and Au@a-TiO_2 (red line in Figure 2a) samples reveal the presence of the Au (111) reflection at a 2θ value of 39°. No peaks related to anatase or rutile or brookite TiO_2 were detected, suggesting that the ALD deposited TiO_2 is primarily amorphous and lacks long-range order. An ALD deposited TiO_2 on a glass substrate sample was annealed at 450 °C for 2 hours to verify the induction of crystallinity with elevated temperature processing. The XRD pattern of the annealed ALD TiO_2 sample (blue line in Figure 2a) shows all the peaks corresponding to anatase phase, thus proving that the annealing does indeed change the structure of the ALD TiO_2 from amorphous to crystalline. Another powerful tool for investigating ordered/disordered TiO_2 structures is Raman spectroscopy.[19] The Raman spectra of the a-TiO_2, annealed crystalline anatase TiO_2 and Au@a-TiO_2 samples are shown in Figure 2b. Due to the absence of long-range order, the characteristic phonon modes of anatase are extremely

weak in a-TiO_2 (black curve in Figure 2b). The annealed anatase phase TiO_2 sample (blue curve in Figure 2b) exhibited an intense peak at *ca.* 145 $cm^{-1,}$ which belongs to the Eg mode with three less intense peaks at 395 cm^{-1}, 516 $cm^{-1,}$ and 640 cm^{-1} which belong to B1g, A2g, and Eg modes, respectively. Compared to the annealed sample, the Au@a-TiO_2 (red curve in Figure 2b) exhibited less intense peaks at the same wavenumbers, which indicates that a-TiO_2 is disordered and may possess some short range order at best.[20] The chemical composition and corresponding binding energies of the Au@a-TiO_2 sample were investigated by X-ray photoelectron spectroscopy (XPS). The XPS elemental survey scan shows the presence of Ti2p, Ti2s, O1s, Au 4f and Au 4d peaks (Figure S3a), which evidences all the elements of Au and TiO_2. Deconvoluted peaks of the high-resolution XPS scan in the O1s region exhibit three peaks centered at 530.2 eV, 531.1 eV, and 532.4 eV. These peaks correspond to Ti-O, oxygen vacancies (V_O), and surface chemisorbed oxygen (C_O) repsectively.[21-23] Similarly, the decomposition of the peaks at the Ti2p region exhibits two major peaks centered around 459 eV and 465 eV, which can be attributed to $Ti2p_{3/2}$ and $Ti2p_{1/2}$ of Ti^{4+} in TiO_2 crystal structure, respectively.[24, 25] The presence of gold in the Au@a-TiO_2 sample was confirmed using two deconvoluted peaks at 84 eV and 87.6 eV, which were assigned to $Au4f_{7/2}$ and $Au4f_{5/2,}$ respectively.[26] Figure S3e depicts the XPS depth profile of elements of interests (Ti, Au, and Sn) of the Au@a-TiO_2 photoelectrode to track the presence of a-TiO_2, Au, and SnO_2 respectively as a function of etch depth. For the depth profile scan, the $Ti2p_{3/2}$ peak was used to track the abundance of a-TiO2, $Au4f_{5/2}$ to track the abundance of Au and Sn_{3d} to track the presence of FTO. The core@shell architecture of the Au@a-TiO_2 heterojunction is evidenced by this depth profile scan in which the outer surface is completely covered with ALD deposited amorphous TiO_2. As the sputter etching continues, the abundance of the Au increases. The depth profile also confirms that the ALD deposition of amorphous TiO_2 layer was successful in covering

the area of the FTO surface, which was exposed after annealing (dewetting) of the sputtered Au film as Ti could be found even near the surface of FTO (shown by the abundance of the Sn in the XPS depth profile). In the Au@a-TiO_2 core-shell photoanodes, the Au nanoparticles are never in direct contact with the electrolyte. In this case, the Au core solely acts as an optical antenna and does not directly oxidize or reduce hydroxyl ions or protons in the water splitting reaction.[27] As a result, the amorphous ALD deposited TiO_2 plays the dual role of a charge carrier acceptor and protective layer.[28]

2.2 Photoelectrochemical performance of Au@a-TiO_2 photoanode

The ultrathin Au@a-TiO_2 core-shell nanoparticle photoanode proved itself to be an excellent photoanode for the sunlight-driven splitting of water (Figure 3). As previously shown (in Figure 1c) and discussed, the Au@a-TiO_2 photoelectrode exhibits appreciable light absorption in the visible light region *i.e.* photons of wavelength >420 nm. The photocurrent response of Au@a-TiO_2 in comparison with the a-TiO_2 layer was investigated using linear sweep voltammetry (LSV) under excitation of 1 sun as well as ultraviolet-filtered visible light (under AM1.5G 1 Sun with a 420 nm long pass filter). Under AM1.5G 1 Sun illumination, Au@a-TiO_2 revealed a remarkable photoresponse of 2.5 mA cm^{-2} while the photoresponse of a-TiO_2 was only 0.3 mA cm^{-2}. The photoelectrochemical performance of the Au@a-TiO_2 core-shell photoanode is impressive in both relative and absolute terms. Even several micrometer-thick films of traditional *n*-type semiconductor photoanodes made of TiO_2, anion-doped TiO_2, $SrTiO_3$, Fe_2O_3 and g-C_3N_4/TiO_2 have only been able to generate 1.8-2 mA cm^{-2} of photocurrent under AM1.5G 1 sun illumination. Therefore, the ability of the Au@a-TiO_2 to not merely match but exceed this performance is impressive, and doubly impressive when the ultrathin nature of the photoanode (<60 nm in thickness) is taken into account. Under both 1 sun and UV filtered 1 sun illumination, the

photoresponse of Au@a-TiO_2 is almost 8.3 and 5 times that of the a-TiO_2 photoelectrode under identical conditions, conclusively demonstrating the dominant role of Au and plasmonic hot carriers in the water oxidation process. These results can be understood by recognizing that interband damping is a dominant plasmon dephasing mechanism for Au NPs sized 25-75 nm used in this work (Figure S2a), contributing more than half of the observed homogeneous linewidth broadening.[29] Consider the behavior of hot carrier pairs formed by interband damping of the Au surface plasmon excited by high energy (λ < 420 nm) photons. Ultrafast transfer of hot electrons from Au nanoparticles to indium tin oxide (ITO) coated glass substrates is known,[30] and there is every reason to expect comparable or faster hot e- transfer from Au@a-TiO_2 core-shell nanoparticles to the FTO substrate in this work considering the similar electronic properties of ITO and FTO, and the higher roughness of FTO compared to ITO (enhanced local E-fields and more numerous hot spots). Hot holes in Au are transferred to trap levels of a-TiO_2 where a nonthermal distribution of carriers is maintained resulting in the reduction of thermalization losses.[31] The thin a-TiO_2 shell is electron rich under AM1.5G 1 sun illumination due to excitation by UV photons and the simultaneous inability to transfer electrons to protons at the surface (the TiO_2 surface is deprotonated in 1 M KOH). Consequently, the already electron rich a-TiO_2 shell is unable to accept further hot electrons from Au, which accounts for the seemingly unidirectional flow of hot holes from Au into TiO_2 under AM1.5G 1 sun illumination. We measured the hydrogen resulting from water-splitting using a H-Cell (experimental details in Supporting Information), and the results are shown in Figure 3b. Under 1 sun illumination, the Au@a-TiO_2 exhibits a remarkable H_2 production rate of 22.8 μmol h^{-1} (corresponding to a Faradaic efficiency of ~79%) which is almost ten times larger than the H_2 production rate of a-TiO_2 photoelectrode (2.6 μmol h^{-1}).

The stability of the photoelectrode is an important factor for PEC water splitting applications. The variation of the photocurrent as a function of time (*I-t* curve) can be used as a figure of merit for a photoelectrode's stability.[32] The *I-t* curves of the Au@a-TiO_2 and a-TiO_2 photoelectrodes at an applied bias of +0.6 V versus the Ag/AgCl counter electrode are shown in Figure 3a. It is seen that the Au@a-TiO_2 samples exhibited a stable photoresponse during 3-minute irradiation steps.

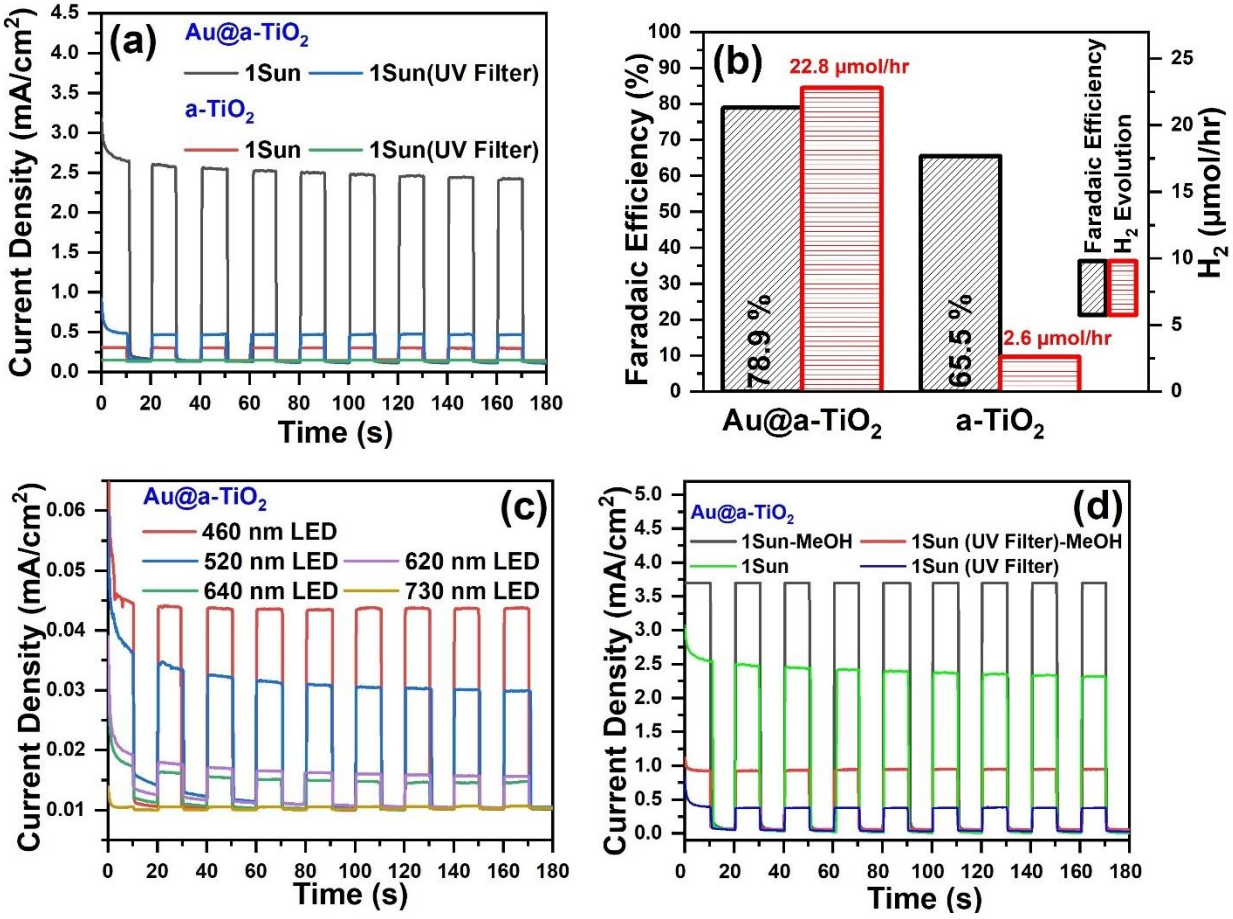

Figure 3. (a) Photoelectrochemical measured it curves of Au@a-TiO_2 and a-TiO_2 using the solar simulator and solar simulator with UV cut-off illumination under +0.6 V applied potential vs. Ag/AgCl reference electrode in a 1M KOH electrolyte (b) Corresponding H_2 evolution and Faradaic efficiency of Au@a-TiO_2 under solar simulator illumination. (c) Photoelectrochemical measured I-t curves of Au@a-TiO2 using visible LEDs illumination under +0.6 V applied potential vs. Ag/AgCl reference electrode in a 1M KOH electrolyte (D) comparison between the photoelectrochemical measured I-t curves of Au@a-TiO_2 using the solar simulator and solar simulator with UV cut-off illumination under

+0.6 V applied potential vs. Ag/AgCl reference electrode in a 1M KOH electrolyte with and without hole scavengers (MeOH).

2.3 Processes underlying the photoelectrochemical performance of Au@a-TiO_2 photoanodes

Figure S4a shows that the dark current was small (< 0.45 $mAcm^{-2}$) for Au@a-TiO_2 and negligible small (<0.02 $mAcm^{-2}$) for a-TiO_2. TiO_2 has a large concentration of trapped holes at the surface which are subject to nucleophilic attack by water molecules. The onset potential for the flow of positive anodic current through the a-TiO_2 electrode was -0.88 V vs Ag/AgCl in the dark and shifted to -0.98 V vs Ag/AgCl under AM1.5G 1 sun illumination, which is consistent with prior reports on TiO_2 based photoanodes in highly basic electrolytes. The magnitude of the anodic current is limited by the poor hole mobility of disordered a-TiO_2 which limits replenishment of the holes captured by water molecules. On the other hand, the onset potential for Au@a-TiO_2 is -0.49 V vs Ag/AgCl in the dark and shifts to -0.72 eV under AM1.5G 1 sun illumination, and the corresponding anodic currents are larger by an order of magnitude. This indicates the number of trapped holes to be smaller on the surface of Au@a-TiO_2 likely due to charge transfer from TiO_2 to Au during the junction formation and equilibration. The injection of holes from Au into disordered TiO_2 under positive anodic bias causes trap-filling and a higher effective hole mobility in the a-TiO_2 shell around the Au resulting in larger anodic currents in both the dark and under 1 sun illumination. One interesting observation is the significant decrease in the magnitude of the photovoltage and anodic photocurrent of Au@a-TiO_2 samples when UV-filtered visible light is incident. The onset potential and anodic current density (at +0.6 V) bias are -0.25 V vs Ag/AgCl and 0.47 $mAcm^{-2}$ respectively. We attribute this decrease to the bidirectionality of charge flow during visible light illumination. a-TiO_2 is not excited by visible light illumination and therefore does not possess excess electrons. Hot electrons generated by intraband damping of Au plasmons are injected into both the a-TiO_2 shell and FTO substrate. Hot holes are still injected from Au into

a-TiO_2 albeit fewer in number than for UV excitation due to weaker interband damping of plasmons excited by lower energy photons. This is because the minimum threshold energy for interband damping in Au is 2.3 eV and the probability of interband transitions sharply decreases below ~2.4 eV.[33] The hot electrons and hot holes injected into a-TiO_2 recombine causing a reduction in both the anodic photovoltage and photocurrent density under UV-filtered solar illumination. However, the photocurrent density remains positive (anodic) indicating that the number of holes injected from Au into a-TiO_2 still exceeds the number of injected electrons. This type of wavelength-dependent directionality and magnitude of carrier flow in Au-TiO_2 heterojunctions has been previously reported by us and others in the context of CO_2 photoreduction[14] but is novel in the context of photoelectrochemical water splitting.

Investigation of the visible light photocurrent generation of Au@a-TiO_2 sample was conducted using a set of LEDs with emission centered at 460 nm, 520 nm, 620 nm, 640 nm, and 730 nm, each with a bandwidth of 10 nm. The LSV and *I-t* curves using this set of LEDs are shown in Figure S4b and Figure 3c respectively. The photocurrent was anodic under the excitation of each of these LEDs. Au@a-TiO_2 showed the highest photoresponse under 460 nm excitation. The photoresponse gradually decreased with increasing wavelength. Another figure of merit for evaluation of plasmon-induced PEC water-splitting is the photocurrent measurement as a function of excitation wavelength, also known as the action spectrum.[34, 35] Figure 4a depicts the corresponding visible light action spectrum of the Au@a-TiO_2 photoanode using the *I-t* curves (the absorption spectrum of Au@a-TiO_2 in the visible light region is also shown by a dotted blue line to guide the eyes). The action spectra of the Au@a-TiO_2 photoanode did not follow the LSPR peak and showed a gradual decrease as the wavelength increased. This is characteristic of plasmonic photocatalysts where interband damping of the plasmon is the dominant source of hot

carrier generation. When intraband damping is the primary generator of hot carriers, the action spectrum has the same profile as the LSPR optical extinction spectrum. To further elucidate charge transfer phenomena in the Au@a-TiO_2 photoanode, we utilized scanning Kelvin probe force microscopy (KPFM) to measure the surface potential of the samples.[36, 37] To analyze the viability of the injection of hot holes from Au into the outer a-TiO_2 shell, the surface potential of Au@a-TiO_2 photoelectrode was measured using KPFM under two illumination sources of 520 nm and 635 nm. The results are shown in Figure 4b. Since the a-TiO_2 shell is the outer layer in Au@a-TiO_2 sample, the KPFM result is the representation of the potential of the shell (a-TiO_2). According to Figure 4b, when Au@a-TiO_2 is subjected to 635 nm and 520 nm excitations, the surface potential is shifted to positive side in each case compared to the dark condition. Interestingly, the 520 nm excitation resulted in a more positive surface potential compared to 635 nm illumination of identical power and the dark, which is in good agreement with the action spectrum graph in which the photocurrent generation was higher for excitation by higher energy photons, further confirming the role of interband damping and hot hole extraction by TiO_2. Methanol, a known hole scavenger, was used in the electrolyte (see Materials and Methods in Supporting Information) to quickly react with photogenerated holes in Au@a-TiO_2 before they recombine.[38] Figure 3d shows the *I-t* curves of Au@a-TiO_2 photoanode using methanol as the hole scavenger. A large photocurrent enhancement effect was seen when methanol was used in the electrolyte as a hole scavenger under the excitation of 1 Sun and visible light (using the UV cut-off filter). This further proves that the fabricated Au@a-TiO_2 photoelectrode supplies photogenerated holes to the electrolyte during the water-splitting reaction. While the adsorbed water and hydroxyl ions are known to react with mobile holes, methanol is also capable of reacting with immobile trapped holes in TiO_2.[39, 40] Therefore, the increase in photocurrent density at anodic bias of 0.6 V under

AM1.5G one sun illumination due to the addition of methanol from 2.5 to 3.7 $mAcm^{-2}$ (Figure 3d), is mainly due to more efficient extraction of holes from the surface of Au@a-TiO_2.

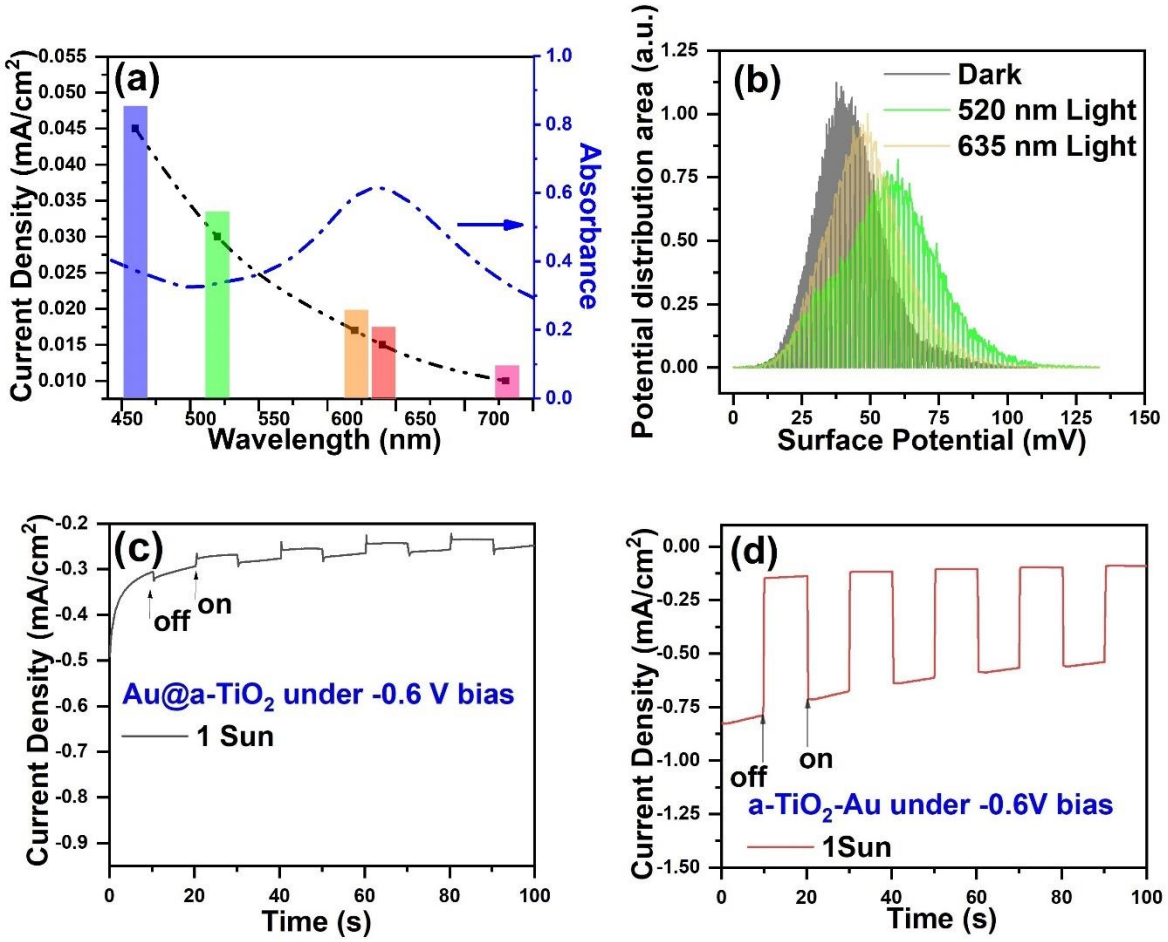

Figure 4. (a) Corresponding action spectrum of Au@a-TiO_2 under LEDs illumination. (b) The surface potential of the Au@a-TiO_2 photoelectrode under 520 nm and 635 nm excitations. (c) Measured *i-t* curves of Au@a-TiO_2 using solar simulator under -0.6 V applied potential vs. Ag/AgCl reference electrode in a 1 M Na_2SO_4 electrolyte (d) Measured it curves of a-TiO_2- Au using solar simulator under -0.6 V applied potential vs. Ag/AgCl reference electrode in a 1 M Na_2SO_4 electrolyte.

Methanol, a known hole scavenger, was used in the electrolyte (see Materials and Methods in Supporting Information) to quickly react with photogenerated holes in Au@a-TiO_2 before they recombine.[38] Figure 3d shows the *I-t* curves of Au@a-TiO_2 photoanode using methanol as the hole scavenger. A large photocurrent enhancement effect was seen when methanol was used in the

electrolyte as a hole scavenger under the excitation of 1 Sun and visible light (using the UV cut-off filter). This further proves that the fabricated Au@a-TiO_2 photoelectrode supplies photogenerated holes to the electrolyte during the water-splitting reaction. The principal mechanism for the increase in photocurrent density for the Au@a-TiO_2 photoanode from 2.5 to 3.7 $mAcm^{-2}$ upon methanol addition to the electrolyte is the current doubling effect.[41] The current doubling effect occurs to due to methanol molecules accepting a hole from the valence band of a *n*-type semiconductor photoanode and then also injecting electrons into the conduction band of the photoanode.[42] While the adsorbed water and hydroxyl ions are known to react with mobile holes, methanol is also capable of reacting with immobile trapped holes in TiO_2.[39, 40] Therefore, the increase in photocurrent density at anodic bias of 0.6 V under AM1.5G one sun illumination due to the addition of methanol from 2.5 to 3.7 $mAcm^{-2}$ (Figure 3d), is due to the current doubling effect as well as more efficient extraction of holes from the surface of Au@a-TiO_2.

Two sets of complementary experiments were conducted to study the charge transfer mechanism in the Au@a-TiO_2 photoelectrodes. Firstly, instead of using the Au@a-TiO_2 as a photoanode (applying positive +0.6 V bias to the photoelectrode), this heterostructure was used as a photocathode by applying a negative bias to it (-0.6 V). Figure 4c exhibits the AM1.5 1 sun photocurrent repose of this photoelectrode under negative bias. Interestingly, the results show a weak anodic photocurrent which means that even under applied negative bias to the Au@a-TiO_2 photoelectrode, Au nanoparticles are still injecting the holes to the outer a-TiO_2 shell. This indicates an unusually strong driving force. Secondly, the architecture of the Au@a-TiO_2 was reversed by changing the sequence of deposition of a-TiO_2 and Au (the thin amorphous layer of TiO_2 was deposited on the FTO substrate at first, and then the Au film were sputtered on top of it). This photoelectrode was named as a-TiO_2-Au photoelectrode. In this case, the Au nanoparticles

are only in direct contact with the thin amorphous TiO_2 layer and not with the FTO. Interestingly, when the applied voltage was -0.6 V against the reference electrode, the a-TiO_2-Au photoelectrode exhibited cathodic photocurrent (Figure 4d), which indicates the injection of holes into the a-TiO_2 layer and driving the reduction reaction at the interface of the a-TiO_2-Au and the electrolyte, these results again confirm the possibility of the injection of holes into the thin amorphous TiO_2 layer. Overall, the action spectrum measurement, electron/hole scavenger tests, along with KPFM, NIR UV-vis spectra, and changing the architecture of the Au@a-TiO_2 photoelectrode are well aligned with each other and suggest the injection of hot holes into the outer a-TiO_2 shell.

The Mott-Schottky plot for a-TiO_2 (Figure S6c in Supporting Information) exhibits the typical positive slope of an *n*-type semiconductor. The carrier concentration for a-TiO_2 was estimated to be 10^{20}- 10^{21} cm^{-3} which is relatively high, and further supports the presence of oxygen vacancies in a-TiO_2 indicated by the XPS data. While 10 nm-thick films are usually unable to support band-bending due to insufficient charge available to be depleted, the high self-doping of a-TiO_2 film renders it capable of forming a depletion region. The Mott-Schottky plot of Au@a-TiO_2 showed an increase in positive slope which corresponds to a lower carrier concentration and the formation of a wider depletion region with an estimated 3-10 nm width. The ultraviolet photoelectron spectra (UPS) of Au, a-TiO_2, and Au@a-TiO_2 are shown in Figure S6a in Supporting Information. The work function (ϕ_s) of Au, a-TiO_2, and Au@a-TiO_2 photoelectrodes were calculated to be 4.61 eV, 3.5 eV, and 3.81 eV respectively using the expression $\phi_s = h\nu - E_{SE}$ in which $h\nu$ is the energy of the photons used to investigate the band structure (21.21 eV) and E_{SE} is the secondary electron cut-off energy.[43] The low work function of amorphous TiO_2 is a result of strong *n*-type behavior and bandgap widening. The bandgap of very thin, amorphous ALD-grown TiO_2 films has been reported to be as high as 3.8 eV due to a combination of carrier localization and quantum

confinement effects.[44, 45] UPS is an extremely surface-sensitive technique with a depth resolution of a few monolayers (~1-2 nm). Gold is not exposed at the surface of Au@a-TiO_2 samples. Therefore, the work-function measured for Au@a-TiO_2 is that of the a-TiO_2 shell covering the gold. The measured work function of 3.81 eV for Au@a-TiO_2 indicates a deeper Fermi level in a-TiO_2 due to depletion of electrons and the formation of a Schottky junction with Au. The valence band maxima of a-TiO_2 and Au@a-TiO_2 are located 3.5 eV and 3.27 eV respectively below the Fermi level (Figure S6b in Supporting Information). The decrease in the valence band maximum for the Au@a-TiO_2 photoelectrode compared to a-TiO_2 indicates upward band bending at the Au/a-TiO_2 interface and confirms the formation of a Schottky junction.[43]

Excess carriers in amorphous or partially crystalline TiO_2 can have unusually long lifetimes extending to several hours due to the high dielectric relaxation time and the low probability of direct recombination of trapped holes with trapped electrons, which manifests itself in persistent photoconductivity (PPC).[45, 46] The practical implication of PPC for plasmonic photocatalysis is that once hot carriers are injected from Au into the thin a-TiO_2 shell and subsequently captured by deep traps in TiO_2, the resulting carrier distribution is nonthermal and can remain that way for relatively long durations (minutes to hours). This enables hot holes injected from Au into TiO_2 to remain hot and results in a reduction of thermalization losses together with a concomitant increase in photovoltage and thermodynamic driving force for water oxidation.[31] Prior reports indicate that long-lived excess carriers in TiO_2 injected from gold can be detected through the increased near-infrared (NIR) absorption of free carriers.[14] To investigate if such long-lived excess carriers are also present in Au@a-TiO_2, the UV-Vis spectra of the Au@a-TiO_2 from ultraviolet to near-infrared (NIR) region were recorded before and after 1 hour of visible light illumination (Figure S6d). The illumination with visible light excites the LSPR of Au nanoparticles and subsequent

plasmon decay is followed by hot electron injection into both FTO and TiO_2, and hole injection into TiO_2. On a net basis, TiO_2 receives an excess of holes and FTO receives an excess of electrons as indicated by the previously discussed KPFM data. A large percentage of the injected carriers of both polarities will likely be captured by deep level traps in TiO_2 and the resulting trap filling will also increase the overall concentration of mobile carriers. Indeed, Figure S6d shows an increase in the NIR absorption due to a larger population of mobile carriers. The inset of Figure S6d exhibits the difference between the LSPR peak-normalized UV-vis spectra of Au@a-TiO_2 before and after visible light illumination. Interestingly the normalized difference spectra show a dip around 1750 nm which is probably due to an excess carrier-mediated shift in the plasmon resonance of FTO which is known to occur between 1500-2100 nm.[47, 48]

When the size of the plasmonic nanoparticle is <100 nm in an LSPR excited plasmonic metal /semiconductor heterojunction, there are two possible ways that the charge can transfer between the excited plasmon and the semiconductor, the first way is the plasmon resonance energy transfer (PRET) occurring over longer ranges, and the second one is short range hot-carrier injection.[34, 49, 50] We have made a strong case in this work for interband damping-mediated hot hole injection from Au into TiO_2 under AM1.5G one sun illumination. Now, we will rule out the possibility of PRET occurring in Au@a-TiO_2. In PRET, the plasmon energy directly transfers to the nearby semiconductor and creates electron-hole pairs in the conduction and valence bands of the semiconductor respectively. The main prerequisite for the PRET is the spectral overlap between the plasmon band of the metal and the absorption band of the semiconductor.[51] Based on the UV-vis spectra, such overlap does not exist in the Au@a-TiO_2 sample; the PRET mechanism is therefore not valid in the Au@a-TiO_2 case, narrowing the possible mechanism of charge transfer to hot-carrier injection mechanism. The hot-carrier injection mechanism's precondition is the direct

contact between the metal and the semiconductor, which is valid for the fabricated Au@a-TiO_2 sample.[51]

To provide evidence that a-TiO_2 is an integral entity in Au@a-TiO_2 photoelectrode, two supplementary experiments were conducted. In the first measurement, the a-TiO_2 shell was replaced with Al_2O_3 (Au@Al_2O_3). Figure S7a exhibits *I-t* curves of the Au@Al_2O_3 under 1 sun and 1 sun with UV filter illumination. It is evident that coating the surface with an insulator dramatically decreased the photocurrent. In the next experiment, the Au@a-TiO_2 was annealed at 500°C to induce crystallinity. This sample was named Au@c-TiO_2, *I-t* curves of this sample for 1 sun and 1 sun with UV filter illumination are shown in Figure S7b. The Au@c-TiO_2 exhibited 1.75 mA Cm^{-2} and 0.25 mA $Cm^{-2,}$ which is a large decrease in photoelectrochemical performance compared to the photocurrent values obtained using Au@a-TiO_2. These experiments verify that the a-TiO_2 is an essential component in the Au@a-TiO_2. Its amorphous nature facilitates hot hole harvesting in Au@a-TiO_2 photoelectrode and dramatically enhances the photoresponse of this electrode.

2.4 DFT modeling results

To gain further insight into the band structure of the Au@a-TiO_2 photoelectrodes, DFT calculations were performed for this heterostructure (see Materials and Methods section in Supporting Information for details of the DFT calculations). DFT is a powerful tool to gain insight into the projected density of states (PDOS) in the system under consideration.[37] In order to find the band structure of the heterojunction, the molecular orbitals are found for when Au and a-TiO_2 are a fair distance apart ("far" configuration) and for when Au and TiO_2 are in intimate contact ("close" configuration). Figure 5 depicts the PDOS of the simulated Au@a-TiO_2 heterostructure in intimate contact, and the positions of highest occupied molecular orbital (HOMO) and lowest

unoccupied molecular orbital (LUMO) of Au and a-TiO_2 in the far (Figure 5b) and close (Figure 5c) configurations. From Figure 5b, it is clear that in the far configuration, the HOMO and LUMO are both localized on Au nanoparticles. In the close configuration, the LUMO is spread out on both Au and a-TiO_2 while the HOMO level is mainly localized on Au nanoparticles with small amount of penetration into the a-TiO_2 structure. Such spatial molecular orbital separation is indicative of superior charge separation following excitations. The PDOS calculations showed that a-TiO_2 valence and conduction bands are predominantly composed of oxygen p-orbitals and titanium d-orbitals (Figure 5a), consistent with the reported literature.[52, 53] The PDOS calculations support the formation of defects inside the band gap of a-TiO_2 due to perturbation and oxygen deficiencies.[54] For comparison purposes, the PDOS for an Au-TiO_2 heterostructure without any perturbation and oxygen vacancies was calculated (Figure S8a), which does not show any mid-gap defect states in crystalline TiO_2. Figure S8b shows the orbital resolved PDOS of Au. The occupied states of gold are mainly composed of d-orbitals, while states above the Fermi level are mostly sp-orbitals. The PDOS result also supports the transfer of photoexcited holes from the d band of Au to the defect states of a-TiO_2. The Au 3d extends from -1.5 and -1 eV, and the sp hybridized orbital of Au extends from 0 to 0.6 eV. Based on the PDOS result, under visible light illumination, the electrons are photoexcited from Au 3d to Au sp, leaving holes behind in Au 3d levels which can get injected into a-TiO_2 by a defected assisted process.

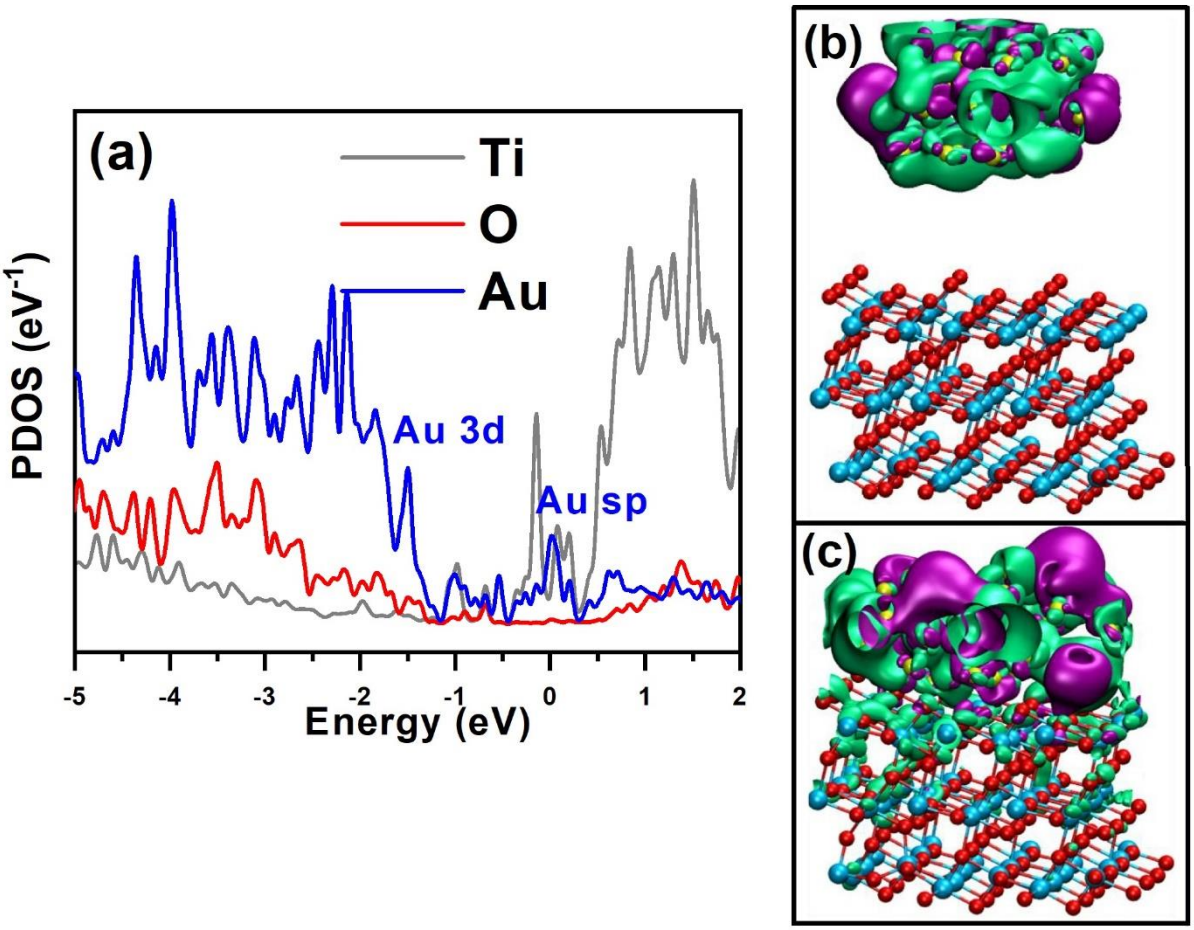

Figure 5. (a) Projected density of states (PDOS) of selected atoms for Au@a-TiO_2 heterostructures. Oxygen-vacant perturbed anatase TiO_2 (101), and Au (111) were chosen for DFT modeling. The DFT optimized structure showing the highest occupied molecular orbital (HOMO) and lowest unoccupied molecular orbital (LUMO) of Au@a-TiO_2 heterostructure in (b) close and (c) far configuration. Purple and green colors are for HOMO and LUMO surfaces, respectively. Ti, O, and Au atoms are in light blue, red, and yellow colors, respectively.

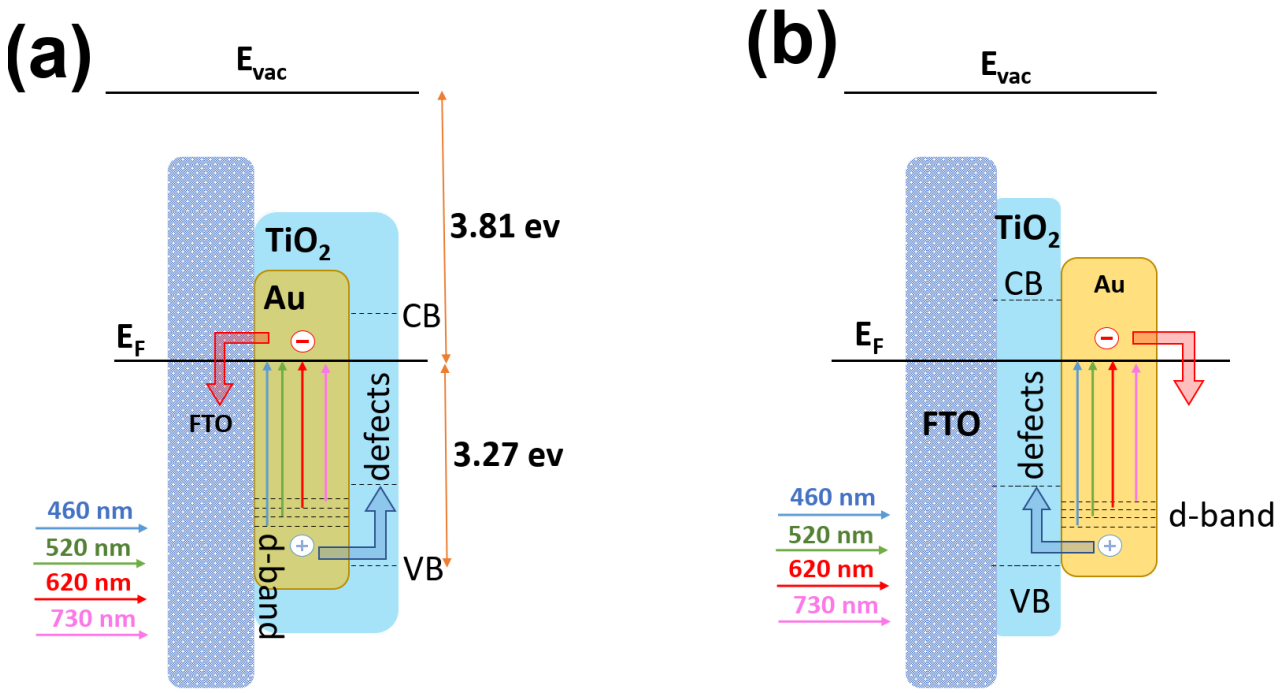

Figure 6. The proposed charge transfer mechanism of (a) Au@a-TiO_2 and (b) TiO2-Au photoelectrodes.

Surface scattering and chemical interface damping are particularly important decay channels for small (<20 nm) coinage metal NPs. For the moderately sized (~50 nm average diameter) Au NPs used in this work, surface scattering and chemical interface damping do not contribute significantly to plasmon dephasing.[29] Interband damping is the dominant damping mechanism in this size range. The mechanism of charge transfer under visible light illumination for both Au@a-TiO_2 and a-TiO_2-Au configurations is depicted in Figure 6. Au is the primary light absorber since FTO is transparent to deep-UV wavelengths and the thickness of TiO_2 is limited to 10 nm. Regardless of application of positive or negative bias to the photoelectrode, when Au@a-TiO_2 is under AM1.5G one sun illumination, it results in the creation of hot holes in the *d* band of Au nanoparticles that are injected into the a-TiO_2 shell through defect states (Figure 6a). The holes in a-TiO_2 participate in oxidation reactions at the photoelectrode/electrolyte interface. The electrons

in this process which form near or above the fermi level of Au, are injected to FTO and flow through the external circuit to the counter electrode (Pt electrode), and drive the reduction of protons. The remarkable photoelectrochemical performance of the Au@a-TiO_2 architecture depicted in Figure 6a indicates to be an excellent photoanode for the water-splitting reaction. For the a-TiO_2-Au architecture (Figure 6b), under visible light irradiation and negative applied potential, a similar process occurs except that this architecture is a superior photocathode. Hot holes form in the d-band of Au. These holes get injected into the thin a-TiO_2 layer underneath the gold nanoislands and are subsequently transferred to FTO and the counter electrode. Electrons accumulated in Au participate in the reduction reaction at the a-TiO_2-Au/electrolyte interface. What is noteworthy is that Au injects hot holes into the a-TiO_2 layer in both cases. The entire focus of research in Au-TiO_2 heterojunctions has been on the extraction of hot electrons to such an extent that most studies in this area do not even consider the possibility of the injection of d-band hot holes formed in Au (upon plasmon decay) into TiO_2.[55] In this context, we provide persuasive evidence for hot hole injection from Au into TiO_2 through photoelectrochemical performance data for different types of illumination, hole scavenger test, surface potential shifts under illumination and DFT modeling. Using the steady-state *i-t* curves shown in Figure 3a to estimate the steady-state incident-photon-to-electron conversion efficiency (IPCE) indicates near-unity quantum yields (see Section S2 in Supporting Information) at 0.6 V anodic bias (vs Ag/AgCl) for high energy photons ($\lambda < 420$ nm). Narang et al. point out in a recent paper that the measured steady-state charge collection efficiencies for hot carrier plasmonic photovoltaic and photoelectrochemical cells remains less than 1%.[3] The results in this work would therefore constitute one of the highest observed charge collection efficiencies in plasmonic photoelectrochemical cells.

3. CONCLUSION

In conclusion, we present a potential solution to the long-standing problem of hot hole extraction from gold nanostructures. Our results demonstrate that a thin amorphous layer of TiO_2 (a-TiO_2) can function both as a hole extraction layer and as a protective layer in PEC water splitting photoelectrodes. This demonstration is contrary to the conventional understanding of TiO_2 exclusively being an excellent electron-accepting material. Highly stable, ultrathin Au@a-TiO_2 photoelectrodes were fabricated by sputtering Au followed by ALD deposition of amorphous TiO_2. The Au@a-TiO_2 photoanodes generated an outstanding photocurrent of 2.5 $mA.cm^{-2}$ under AM1.5G 1 Sun illumination, which is almost 8.3 times higher than an ALD deposited amorphous TiO_2 (a-TiO_2) layer. Addition of a hole scavenger to the electrolyte resulted in the anodic photocurrent increasing to 3.7 $mAcm^{-2}$ for a photoanode with an overall thickness < 100 nm. Such a remarkable photoelectrochemical performance resulted from the successful extraction of hot holes from Au into a-TiO_2. The Au@a-TiO_2 photoelectrode exhibited strong absorption in the visible part of the solar spectrum and enhanced photocurrent generation compared to the a-TiO_2 layer under visible light irradiation. Our work shows that near-unity charge collection efficiencies are achievable in hot carrier driven photoelectrochemical cells for at least select spectral bands in sunlight, and that external quantum yields need not be limited to low single digit values in plasmonic catalysis.

ASSOCIATED CONTENT

Supporting Information.

The following files are available free of charge.

Experimental and Modeling Methods as well as Figures S1−S9 (PDF)

AUTHOR INFORMATION

Corresponding Author

*Email: vahidzad@ualberta.ca

*Email: kshankar@ualberta.ca

Present Addresses

†Dr. Pawan Kumar, Department of Chemical and Petroleum Engineering, University of Calgary, Calgary, AB, Canada T2N 1N4

Author Contributions

The manuscript was written through contributions of all authors. All authors have given approval to the final version of the manuscript.

Notes

The authors declare no competing financial interest.

ACKNOWLEDGEMENT

All authors thank NSERC and Future Energy Systems CFREF for financial support. Indirect (equipment related) support from National Research Council Canada and the Canada Foundation for Innovation are acknowledged. EV acknowledges being part of, and receiving funding from, the Alberta-Technical University of Munich (ATUMS) collaborative training program, which is itself financially supported by NSERC (CREATE program), Alberta Innovates (Strategic Projects program) and DFG. The authors acknowledge use of the vacuum deposition and characterization facilities at the University of Alberta nanoFAB.

REFERENCES

1. Fujishima, A.; Honda, K., Electrochemical Photolysis of Water at a Semiconductor Electrode. *Nature* **1972,** *238* (5358), 37-38.
2. Halmann, M., Photoelectrochemical reduction of aqueous carbon dioxide on p-type gallium phosphide in liquid junction solar cells. *Nature* **1978,** *275* (5676), 115-116.
3. Cortés, E.; Besteiro, L. V.; Alabastri, A.; Baldi, A.; Tagliabue, G.; Demetriadou, A.; Narang, P., Challenges in Plasmonic Catalysis. *ACS Nano* **2020,** *14* (12), 16202-16219.
4. Araujo, T. P.; Quiroz, J.; Barbosa, E. C. M.; Camargo, P. H. C., Understanding plasmonic catalysis with controlled nanomaterials based on catalytic and plasmonic metals. *Current Opinion in Colloid & Interface Science* **2019,** *39*, 110-122.
5. Manuel, A. P.; Shankar, K., Hot Electrons in TiO2–Noble Metal Nano-Heterojunctions: Fundamental Science and Applications in Photocatalysis. *Nanomaterials* **2021,** *11* (5), 1249.
6. Ishii, S.; Shinde, S. L.; Nagao, T., Nonmetallic Materials for Plasmonic Hot Carrier Excitation. *Advanced Optical Materials* **2019,** *7* (1), 1800603.
7. Karaballi, R. A.; Monfared, Y. E.; Dasog, M., Overview of Synthetic Methods to Prepare Plasmonic Transition-Metal Nitride Nanoparticles. *Chemistry – A European Journal* **2020,** *26* (39), 8499-8505.
8. Hubenthal, F., Increased Damping of Plasmon Resonances in Gold Nanoparticles Due to Broadening of the Band Structure. *Plasmonics* **2013,** *8* (3), 1341-1349.
9. Manuel, A. P.; Kirkey, A.; Mahdi, N.; Shankar, K., Plexcitonics - fundamental principles and optoelectronic applications. *J. Mater. Chem. C* **2019,** *7* (7), 1821-1853.
10. Sundararaman, R.; Narang, P.; Jermyn, A. S.; Goddard Iii, W. A.; Atwater, H. A., Theoretical predictions for hot-carrier generation from surface plasmon decay. *Nature Communications* **2014,** *5* (1), 5788.
11. Aslam, U.; Chavez, S.; Linic, S., Controlling energy flow in multimetallic nanostructures for plasmonic catalysis. *Nat. Nanotechnol.* **2017,** *12* (10), 1000.
12. Harutyunyan, H.; Martinson, A. B. F.; Rosenmann, D.; Khorashad, L. K.; Besteiro, L. V.; Govorov, A. O.; Wiederrecht, G. P., Anomalous ultrafast dynamics of hot plasmonic electrons in nanostructures with hot spots. *Nat. Nanotechnol.* **2015,** *10* (9), 770-+.
13. Alam, K. M.; Kumar, P.; Manuel, A. P.; Vahidzadeh, E.; Goswami, A.; Zeng, S.; Wu, W. J.; Mahdi, N.; Cui, K.; Kobryn, A. E.; Gusarov, S.; Song, Y. N.; Shankar, K., CVD grown nitrogen doped graphene is an exceptional visible-light driven photocatalyst for surface catalytic reactions. *2D Mater.* **2020,** *7* (1).
14. Zeng, S.; Vahidzadeh, E.; VanEssen, C. G.; Kar, P.; Kisslinger, R.; Goswami, A.; Zhang, Y.; Mandi, N.; Riddell, S.; Kobryn, A. E.; Gusarov, S.; Kumar, P.; Shankar, K., Optical control of selectivity of high rate CO2 photoreduction via interband or hot electron Z-scheme reaction pathways in Au-TiO2 plasmonic photonic crystal photocatalyst. *Appl. Catal. B-Environ.* **2020,** *267*.
15. Kisslinger, R.; Riddell, S.; Manuel, A. P.; Alam, K. M.; Kalra, A. P.; Cui, K.; Shankar, K., Nonlithographic Formation of Ta2O5 Nanodimple Arrays Using Electrochemical Anodization and Their Use in Plasmonic Photocatalysis for Enhancement of Local Field and Catalytic Activity. *ACS Appl. Mater. Interfaces* **2021,** *13* (3), 4340-4351.
16. Vahidzadeh, E.; Zeng, S.; Manuel, A. P.; Riddell, S.; Kumar, P.; Alam, K. M.; Shankar, K., Asymmetric Multipole Plasmon-Mediated Catalysis Shifts the Product Selectivity of CO2 Photoreduction toward C2+ Products. *ACS Appl. Mater. Interfaces* **2021,** *13* (6), 7248-7258.

17. Pan, H. Q.; Steiniger, A.; Heagy, M. D.; Chowdhury, S., Efficient production of formic acid by simultaneous photoreduction of bicarbonate and oxidation of glycerol on gold-TiO2 composite under solar light. *J. CO2 Util.* **2017,** *22*, 117-123.
18. Ishida, T.; Toe, S.; Tatsuma, T., Stepwise Injection of Energetic Electrons and Holes in Plasmon-Induced Charge Separation. *The Journal of Physical Chemistry C* **2019,** *123* (50), 30562-30570.
19. Smith, K. A.; Savva, A. I.; Deng, C.; Wharry, J. P.; Hwang, S.; Su, D.; Wang, Y.; Gong, J.; Xu, T.; Butt, D. P., Effects of proton irradiation on structural and electrochemical charge storage properties of TiO 2 nanotube electrodes for lithium-ion batteries. *Journal of Materials Chemistry A* **2017,** *5* (23), 11815-11824.
20. Niilisk, A.; Moppel, M.; Pärs, M.; Sildos, I.; Jantson, T.; Avarmaa, T.; Jaaniso, R.; Aarik, J., Structural study of TiO2 thin films by micro-Raman spectroscopy. *Open Physics* **2006,** *4* (1), 105-116.
21. Ghobadi, A.; Ulusoy, T. G.; Garifullin, R.; Guler, M. O.; Okyay, A. K., A heterojunction design of single layer hole tunneling ZnO passivation wrapping around TiO 2 nanowires for superior photocatalytic performance. *Scientific reports* **2016,** *6*, 30587.
22. Ulusoy, T. G.; Ghobadi, A.; Okyay, A. K., Surface engineered angstrom thick ZnO-sheathed TiO 2 nanowires as photoanodes for performance enhanced dye-sensitized solar cells. *Journal of Materials Chemistry A* **2014,** *2* (40), 16867-16876.
23. Zhu, L.; Zeng, Y.; Zhang, S.; Deng, J.; Zhong, Q., Effects of synthesis methods on catalytic activities of CoOx–TiO2 for low-temperature NH3-SCR of NO. *Journal of Environmental Sciences* **2017,** *54*, 277-287.
24. Olowoyo, J. O.; Kumar, M.; Dash, T.; Saran, S.; Bhandari, S.; Kumar, U., Self-organized copper impregnation and doping in TiO2 with enhanced photocatalytic conversion of H2O and CO2 to fuel. *International Journal of Hydrogen Energy* **2018,** *43* (42), 19468-19480.
25. Kim, M.-S.; Chung, S.-H.; Yoo, C.-J.; Lee, M. S.; Cho, I.-H.; Lee, D.-W.; Lee, K.-Y., Catalytic reduction of nitrate in water over Pd–Cu/TiO2 catalyst: effect of the strong metal-support interaction (SMSI) on the catalytic activity. *Applied Catalysis B: Environmental* **2013,** *142*, 354-361.
26. Wu, L.; Li, F.; Xu, Y.; Zhang, J. W.; Zhang, D.; Li, G.; Li, H., Plasmon-induced photoelectrocatalytic activity of Au nanoparticles enhanced TiO2 nanotube arrays electrodes for environmental remediation. *Applied catalysis B: environmental* **2015,** *164*, 217-224.
27. Hoang, C. V.; Hayashi, K.; Ito, Y.; Gorai, N.; Allison, G.; Shi, X.; Sun, Q.; Cheng, Z.; Ueno, K.; Goda, K., Interplay of hot electrons from localized and propagating plasmons. *Nature communications* **2017,** *8* (1), 771.
28. Moehl, T.; Suh, J.; Sévery, L.; Wick-Joliat, R.; Tilley, S. D., Investigation of (Leaky) ALD TiO2 Protection Layers for Water-Splitting Photoelectrodes. *ACS Appl. Mater. Interfaces* **2017,** *9* (50), 43614-43622.
29. Pinchuk, A.; Von Plessen, G.; Kreibig, U., Influence of interband electronic transitions on the optical absorption in metallic nanoparticles. *Journal of Physics D: Applied Physics* **2004,** *37* (22), 3133.
30. Abb, M.; Albella, P.; Aizpurua, J.; Muskens, O. L., All-Optical Control of a Single Plasmonic Nanoantenna–ITO Hybrid. *Nano Letters* **2011,** *11* (6), 2457-2463.
31. Cushing, S. K.; Chen, C.-J.; Dong, C. L.; Kong, X.-T.; Govorov, A. O.; Liu, R.-S.; Wu, N., Tunable Nonthermal Distribution of Hot Electrons in a Semiconductor Injected from a Plasmonic Gold Nanostructure. *ACS Nano* **2018,** *12* (7), 7117-7126.

32. Sreedhar, A.; Reddy, I. N.; Kwon, J. H.; Yi, J.; Sohn, Y.; Gwag, J. S.; Noh, J.-S., Charge carrier generation and control on plasmonic Au clusters functionalized TiO2 thin films for enhanced visible light water splitting activity. *Ceramics International* **2018,** *44* (15), 18978-18986.
33. Zorić, I.; Zäch, M.; Kasemo, B.; Langhammer, C., Gold, Platinum, and Aluminum Nanodisk Plasmons: Material Independence, Subradiance, and Damping Mechanisms. *ACS Nano* **2011,** *5* (4), 2535-2546.
34. Tan, F.; Li, T.; Wang, N.; Lai, S. K.; Tsoi, C. C.; Yu, W.; Zhang, X., Rough gold films as broadband absorbers for plasmonic enhancement of TiO 2 photocurrent over 400–800 nm. *Scientific reports* **2016,** *6*, 33049.
35. Nishi, H.; Tatsuma, T., Mechanistic analysis of plasmon-induced charge separation by the use of chemically synthesized gold nanorods. *The Journal of Physical Chemistry C* **2018,** *122* (4), 2330-2335.
36. Jian, A.; Feng, K.; Jia, H.; Zhang, Q.; Sang, S.; Zhang, X., Quantitative investigation of plasmonic hot-electron injection by KPFM. *Applied Surface Science* **2019,** *492*, 644-650.
37. Zeng, S.; Vahidzadeh, E.; VanEssen, C. G.; Kar, P.; Kisslinger, R.; Goswami, A.; Zhang, Y.; Mahdi, N.; Riddell, S.; Kobryn, A. E., Optical Control of Selectivity of High Rate CO2 Photoreduction Via Interband-or Hot Electron Z-Scheme Reaction Pathways in Au-TiO2 Plasmonic Photonic Crystal Photocatalyst. *Applied Catalysis B: Environmental* **2020**, 118644.
38. Guzman, F.; Chuang, S. S.; Yang, C., Role of methanol sacrificing reagent in the photocatalytic evolution of hydrogen. *Industrial & Engineering Chemistry Research* **2012,** *52* (1), 61-65.
39. Zarifi, M. H.; Farsinezhad, S.; Abdolrazzaghi, M.; Daneshmand, M.; Shankar, K., Selective microwave sensors exploiting the interaction of analytes with trap states in TiO2 nanotube arrays. *Nanoscale* **2016,** *8* (14), 7466-7473.
40. Tamaki, Y.; Furube, A.; Murai, M.; Hara, K.; Katoh, R.; Tachiya, M., Direct Observation of Reactive Trapped Holes in TiO2 Undergoing Photocatalytic Oxidation of Adsorbed Alcohols: Evaluation of the Reaction Rates and Yields. *Journal of the American Chemical Society* **2006,** *128* (2), 416-417.
41. Kalamaras, E.; Lianos, P., Current Doubling effect revisited: Current multiplication in a PhotoFuelCell. *Journal of Electroanalytical Chemistry* **2015,** *751*, 37-42.
42. Halevy, S.; Korin, E.; Bettelheim, A., Enhancement of photoelectrochemical organics degradation and power generation by electrodeposited coatings of g-C3N4 and graphene on TiO2 nanotube arrays. *Nanoscale Advances* **2019,** *1* (10), 4128-4136.
43. Farsinezhad, S.; Sharma, H.; Shankar, K., Interfacial band alignment for photocatalytic charge separation in TiO 2 nanotube arrays coated with CuPt nanoparticles. *Physical Chemistry Chemical Physics* **2015,** *17* (44), 29723-29733.
44. King, D. M.; Du, X.; Cavanagh, A. S.; Weimer, A. W., Quantum confinement in amorphous TiO2 films studied via atomic layer deposition. *Nanotechnology* **2008,** *19* (44), 445401.
45. Nisika; Kaur, K.; Arora, K.; Chowdhury, A. H.; Bahrami, B.; Qiao, Q.; Kumar, M., Energy level alignment and nanoscale investigation of a-TiO2/Cu-Zn-Sn-S interface for alternative electron transport layer in earth abundant Cu-Zn-Sn-S solar cells. *Journal of Applied Physics* **2019,** *126* (19), 193104.
46. Zarifi, M. H.; Mohammadpour, A.; Farsinezhad, S.; Wiltshire, B. D.; Nosrati, M.; Askar, A. M.; Daneshmand, M.; Shankar, K., Time-Resolved Microwave Photoconductivity (TRMC)

Using Planar Microwave Resonators: Application to the Study of Long-Lived Charge Pairs in Photoexcited Titania Nanotube Arrays. *The Journal of Physical Chemistry C* **2015,** *119* (25), 14358-14365.
47. Dominici, L.; Michelotti, F.; Brown, T. M.; Reale, A.; Carlo, A. D., Plasmon polaritons in the near infrared on fluorine doped tin oxide films. *Opt. Express* **2009,** *17* (12), 10155-10167.
48. Kendall, O.; Wainer, P.; Barrow, S.; van Embden, J.; Della Gaspera, E., Fluorine-Doped Tin Oxide Colloidal Nanocrystals. *Nanomaterials* **2020,** *10* (5), 863.
49. Wu, X.; Centeno, A.; Zhang, X.; Darvill, D.; Ryan, M. P.; Riley, D. J.; Alford, N. M.; Xie, F., Broadband plasmon photocurrent generation from Au nanoparticles/mesoporous TiO2 nanotube electrodes. *Solar Energy Materials and Solar Cells* **2015,** *138*, 80-85.
50. Warren, S. C.; Thimsen, E., Plasmonic solar water splitting. *Energy & Environmental Science* **2012,** *5* (1), 5133-5146.
51. Cushing, S. K.; Li, J.; Bright, J.; Yost, B. T.; Zheng, P.; Bristow, A. D.; Wu, N., Controlling plasmon-induced resonance energy transfer and hot electron injection processes in Metal@ TiO2 core–shell nanoparticles. *The Journal of Physical Chemistry C* **2015,** *119* (28), 16239-16244.
52. Pham, H. H.; Wang, L.-W., Oxygen vacancy and hole conduction in amorphous TiO 2. *Physical Chemistry Chemical Physics* **2015,** *17* (1), 541-550.
53. Gutiérrez Moreno, J. J.; Nolan, M., Ab initio study of the atomic level structure of the rutile TiO2 (110)–titanium nitride (TiN) interface. *ACS Appl. Mater. Interfaces* **2017,** *9* (43), 38089-38100.
54. Pan, X.; Yang, M.-Q.; Fu, X.; Zhang, N.; Xu, Y.-J., Defective TiO 2 with oxygen vacancies: synthesis, properties and photocatalytic applications. *Nanoscale* **2013,** *5* (9), 3601-3614.
55. Yu, Y.; Wijesekara, K. D.; Xi, X.; Willets, K. A., Quantifying Wavelength-Dependent Plasmonic Hot Carrier Energy Distributions at Metal/Semiconductor Interfaces. *ACS Nano* **2019,** *13* (3), 3629-3637.